Solar Energy Radiation Measurement with a Low-Power Solar Energy Harvester

Oscar López-Lapeña and Ramon Pallas-Areny

Department of Electronic Engineering
Universitat Politècnica de Catalunya, BarcelonaTech

Corresponding author: Oscar López-Lapeña
E-mail: oscar.lopez@upc.edu

Abstract

Solar energy radiation measurements are essential in precision agriculture and forest monitoring and can be readily performed by attaching commercial pyranometers to autonomous sensor nodes. However this solution significantly increases power consumption up to tens of milliwatts and can cost hundreds of euros. Since many autonomous sensor nodes are supplied from photovoltaic (PV) panels which currents depend on solar irradiance, we propose to double PV panels as solar energy sensors. In this paper, the inherent operation of the low-power solar energy harvester of a sensor node is also used to measure the open circuit voltage and the current at the maximum power point (I_{MPP}), which allows us to determine solar irradiance and compensate for its temperature drift. The power consumption and cost added to the original solar energy harvester are minimal. Experimental results show that the relation between the measured I_{MPP} and solar irradiance is linear for radiation above 50 W/m^2, and the relative uncertainty limit achieved for the slope is ±2.4% due the light spectra variation. The relative uncertainty limit of daily solar insolation is below ±3.6% and is hardly affected by the so called cosine error, i.e. the error caused by reflection and absorption of light in PV panel surface.

Key words: Solar radiation measurement, solar energy harvesting, pyranometer, wireless sensor networks.

1. Introduction

Solar energy radiation is essential in plant physiology and pathophysiology hence its knowledge is fundamental for example, to estimate evapotranspiration (Gocić et al., 2015) (Petković et al., 2015) and to predict infection risk of some fungus diseases (Katsantonis et al., 2017)(Dalla Marta et al., 2008) that are needed to schedule irrigation and fungicide spraying. Solar energy radiation is usually expressed in terms of the energy flux density through a horizontal area (irradiance) and an integrated value over one day (daily solar insolation) fits these applications. For precision agriculture, high accuracy measurements are not required and manufactures recommend the use of photodiode-based pyranometers which are cheaper than thermopile-based pyranometers (Kipp&Zonen, 2018). However, they still cost hundreds of euros and consume some milliwatts hence do not suit low-cost wireless sensor nodes. As an alternative, insolation values in field studies are usually obtained from public weather stations often far away from the crop of interest. This results in errors due to the inhomogeneous solar energy distribution caused by orography, competing vegetation or clouds (Reuter et al., 2005). For extended areas, more reliable in-field data would be better obtained from wireless sensor networks that include solar radiation sensors but this can be thwarted by cost and power consumption constraints (Wang et al., 2006). In order to overcome these constraints, we propose to use the components already integrated into the solar energy harvester of sensor nodes to measure solar radiation too.

During the last decade, small PV panels have been used as low-cost radiation sensors to monitor PV solar plants. Solar irradiance has been deduced from the voltage drop across a resistor biased by a PV panel operating near short-circuit condition (Husain et al., 2011). Short-circuit current is approximately proportional to solar irradiance hence a way to estimate it, but unfortunately the power yield is null at this operating point. Further, the temperature drift of the sensitivity of the PV panel to solar irradiance must be considered. An obvious solution to compensate for temperature drift is to include a temperature sensor (Carrasco et al., 2014)(Mancilla-David et al., 2014)(Ma et al., 2017) but the sensor and its conditioning circuits add cost. An alternative solution is to measure the open-circuit voltage and the short-circuit current

of the PV panel, (Ortiz Rivera and Peng, 2006) and (da Costa et al., 2014). The temperature coefficient of the short-circuit current is positive whereas that of the open-circuit voltage is negative, and both increase with solar irradiance, which leads to a bijective function between them that can be obtained from a physical model for the PV panels. Unfortunately, the calculation is performed by iterative complex algorithms that require DSPs, and current sensors that do not suit low-power solar energy harvesters because of cost and power consumption constraints.

In order to achieve maximum energy from the sun light, low-power solar energy harvesters bias the PV panels at the maximum power point (MPP) which depends on the solar irradiance on the panel surface (G) and temperature (T). These circuits are designed as maximum power point trackers (MPPTs) and are formed by an algorithm to find MPP and a switching converter to bias the panel at this point and transfer the energy to a secondary battery and the load. Fig. 1 shows the block diagram of a MPPT and the typical current vs. voltage curve (I/V) and power vs. voltage curve (P/V) of PV panels. Low-power MPPTs use special control algorithms and switching converters to simplify the implementation and minimize power consumption.

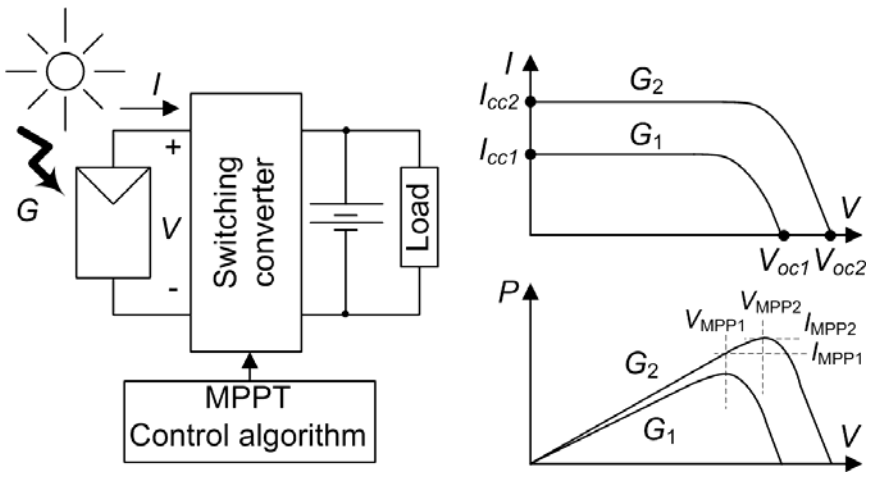

Fig. 1. I/V and P/V characteristics of a photovoltaic panel and a MPPT.

The simplest control algorithm is designed as fractional open circuit voltage (FOCV) and it is based on the empirical relation between the open circuit voltage (V_{oc}) and the voltage at the MPP (V_{MPP}), $V_{MPP} \approx K\, V_{oc}$, where K is a constant that depends on PV panel performance but not on environmental operating

conditions such as temperature or irradiance [Lopez-Lapena, 2016][Rawy, 2017]. FOCV control approximates $V_{MPP}(V_{OC})$ drawn for any temperature and irradiance by a linear regression through the origin. K is the slope of this linear regression.

Fig. 2 shows an algorithm implementation wherein a switch (SW) and a sample & hold (S&H) amplifier periodically disconnect the PV panel and measure V_{oc}, which is then used to calculate V_{MPP}. FOCV implementation in a MCU is easy and the resulting CPU (processor core) workload and power consumption are so small that this is currently the most suitable control algorithm for low-power energy harvesters.

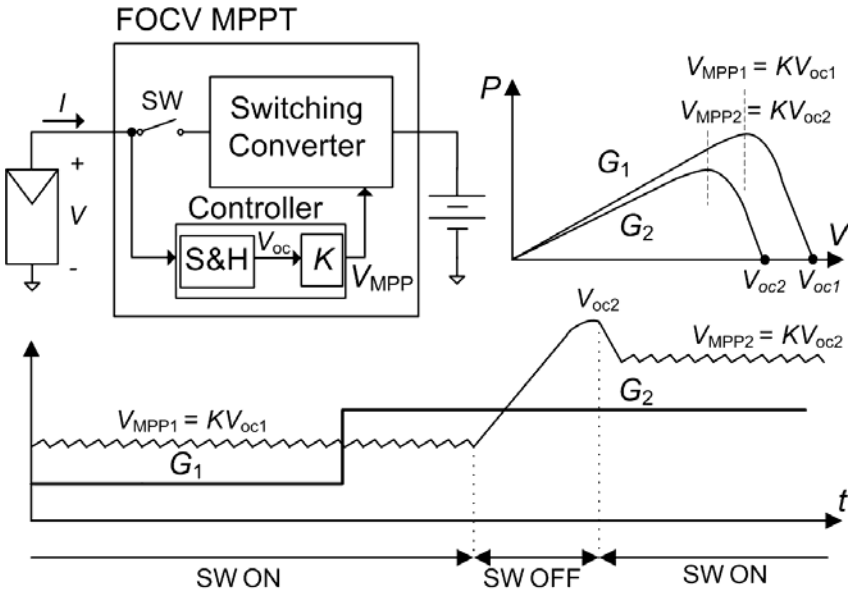

Fig. 2. FOCV control technique.

The energy available in low-power energy harvesters is so scarce that power losses are usually minimized by replacing the classical PWM (pulse width modulation) technique of the switching converter, wherein transistors are continuously switched ON and OFF, by pulse frequency modulation (PFM) [Lopez-Lapena, 2012]. Power losses are reduced by keeping the switching converter inactive while the energy coming from the PV panel is accumulated in an input capacitor (C_{in}). Once charged to a limit value, the switch is activated to discharge C_{in} towards the battery at constant current (I_{ds}), while keeping the input voltage within a hysteresis window (Fig. 3). This way, the energy is not transferred to the battery until the

energy accumulated in the capacitor is much higher than the energy consumption needed to turn on the switching converter; hence achieving a high power efficiency.

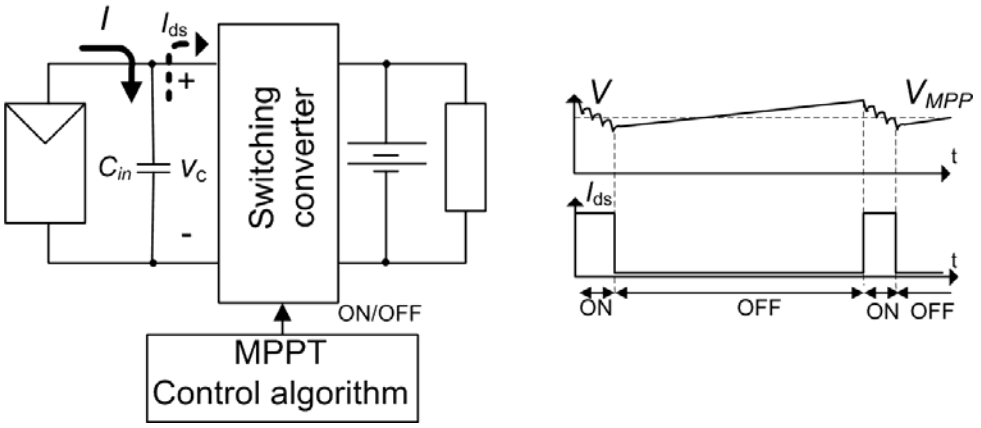

Fig. 3. PFM switching activity.

2. Development of the solar radiation sensor

The proposed solar irradiance sensor relies on a MPPT low-power solar energy harvester based on FOCV algorithm and a PFM switching converter. Solar irradiance and temperature are determined by measuring V_{oc} and the current at MPP (I_{MPP}). V_{oc} measurement is inherent to FOCV operation and I_{MPP} can be easily deduced from the charge duration of the input capacitor C_{in} with PFM.

2.1 Solar energy radiation measurement at constant temperature

The measurement method involves determining the empirical relation between I_{MPP} and G. In order to do that, since for constant light spectrum, temperature and moderate resistive losses, the relation between I_{cc} and G is quite linear, we can easily infer G from I_{cc}. Therefore, we only need to determine the relation between I_{cc} and I_{MPP}. Fig. 4 shows this relation for a SLMD121H04L PV, a 6 cm^2 low-power PV panel, that was illuminated by a high-power LED (BXRA-C1202) with different bias currents (I_{LED}). For I_{MPP} higher than 2 mA, the relation is linear. For lower values, the trace is curved yet includes the point (0,0) which is obtained for zero irradiance resulting in null values for I_{cc} and I_{MPP}.

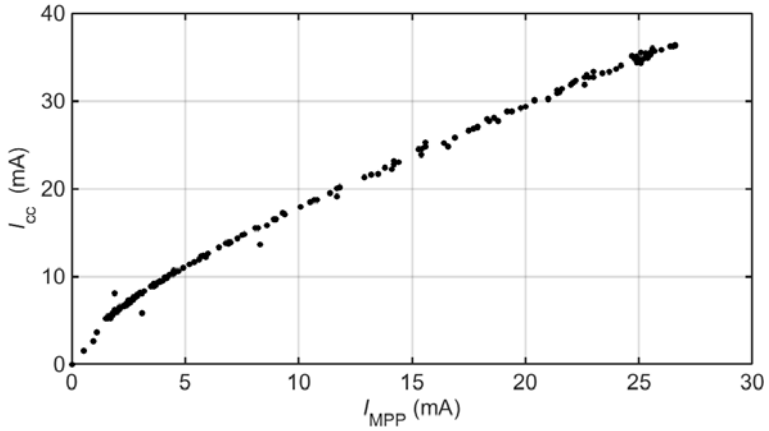

Fig. 4. Measured I_{cc} versus I_{MPP} for a SLMD121H04L PV panel at constant temperature (25ºC).

The nonlinear relation observed in $I_{cc}(I_{MPP})$ around the origin is basically due to the variation of the light-sensitive area of PV panels. This area is defined by the space-charge-region of the PN junctions that constitute the panel. At lower irradiance levels, the resulting I_{MPP} and V_{MPP} are lower and this area is wider, which increases the sensitivity, hence the slope, of $I_{cc}(I_{MPP})$. However, V_{MPP} is almost constant at high irradiance levels by holding a fixed bias voltage of PN junctions and hence a fixed space-charge-region.

2.2 Temperature drift compensation

To study the temperature drift of I_{MPP}, the PV panel was attached to a Peltier cell (MCPF-031-10-25) to undergo a temperature sweep from 6 °C to 70 °C in seven steps. Fig. 5 shows I_{MPP} vs. V_{oc}.

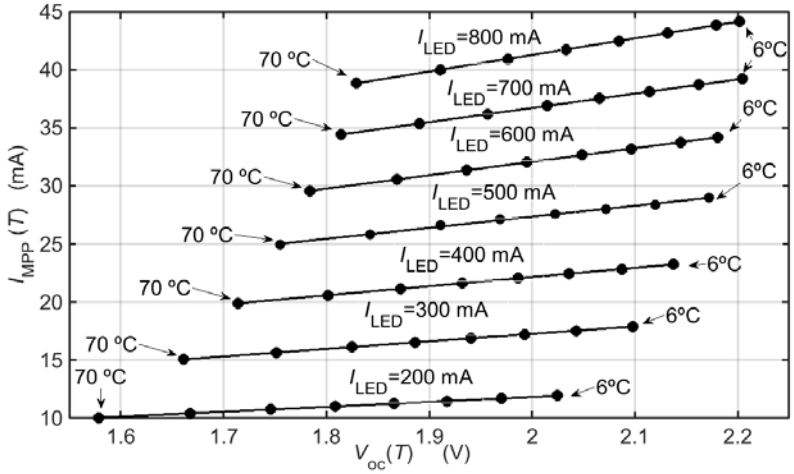

Fig. 5. Temperature dependence of I_{MPP} for SLMD121H04.

From these measurements, a straight line was fitted for each I_{LED} value which fitting parameters are β and α

$$I_{\mathrm{MPP}}(T) = \beta + \alpha V_{\mathrm{oc}}(T). \tag{1}$$

β and α linearly depend on I_{MPP} measured at 25 ºC (Fig. 6). The fitting parameters α_0, α_R, β_0 and β_R depend on PV performance but not on T and G. From these equations, I_{MPP} at 25 °C can be calculated as a function of I_{MPP} and V_{oc} measured at any T,

$$I_{MPP}(25°C) = \frac{I_{MPP}(T) - \beta_0 - \alpha_0 V_{oc}(T)}{\beta_R + \alpha_R V_{oc}(T)} \tag{2}$$

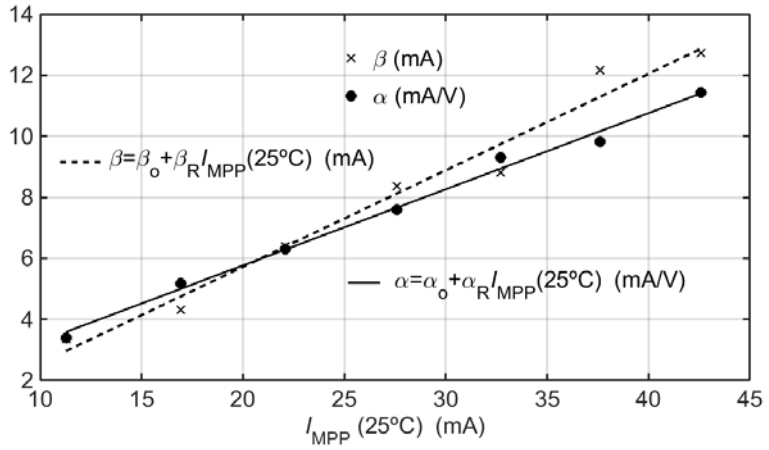

Fig. 6. Dependence of β and α on I_{MPP} (25°C).

The best-fitting parameters according to the least-squares criterion are $\alpha_0 = 0.7734$ mA/V, $\alpha_R = 0.2568\ \mathrm{V}^{-1}$, $\beta_0 = -0.6054$ mA and $\beta_R = 0.3163$.

Fig. 7 shows $I_{\mathrm{MPP}}(25°\mathrm{C})$ calculated from (2) at several T and G operating conditions. Equation (2) provides temperature drift compensation from the measured I_{MPP} and V_{oc} by a simple calculation.

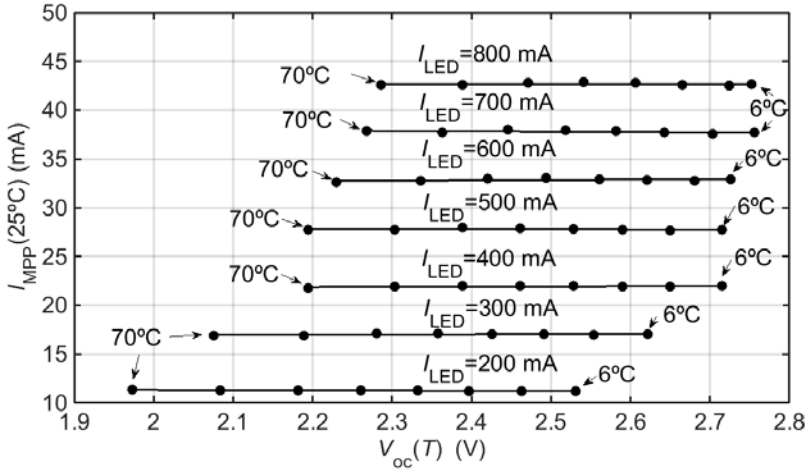

Fig. 7. Temperature compensation of I_{MPP}.

2.3 Circuit implementation

Fig. 8 shows the circuits that implement the FOCV- and PFM-based MPPT and measure I_{MPP} and V_{oc}. A commercial low-power switching converter (MAX1797 and a 10 μH inductor) transfers the energy from a 660 μF input capacitor (C_{in}) to three series-connected NiMH batteries when the shutdown input (SHDN) is '0'. A voltage comparator built from an op amp (EL8176) and four resistors (10 MΩ and 390 kΩ), and a low-power clock (XT1) are used to tell the MCU when to finish and start the discharge cycle of C_{in}. An embedded digital-to-analog converter (output AOUT1) sets the low discharge limit hence the bias voltage of the PV panel. An analog-to-digital converter (AIN1 input) measures the open circuit voltage (V_{oc}) to calculate V_{MPP} and the high hysteresis level of C_{in} bias voltage (v_c). Another analog input (AIN2 input) measures the battery voltage and stops energy transfer when the battery overcharge threshold is reached. When the battery is in overcharge condition, the PV panel must be kept at MPP to measure I_{MPP} but energy transfer must be stopped. This is performed by transistor M1 (IRLML0030TRPBF) that discharges the input capacitor through R_{CAL} and converts the electrical energy into heat. M1 and R_{CAL} are the only components that must be added to the original energy harvester in order to measure solar radiation.

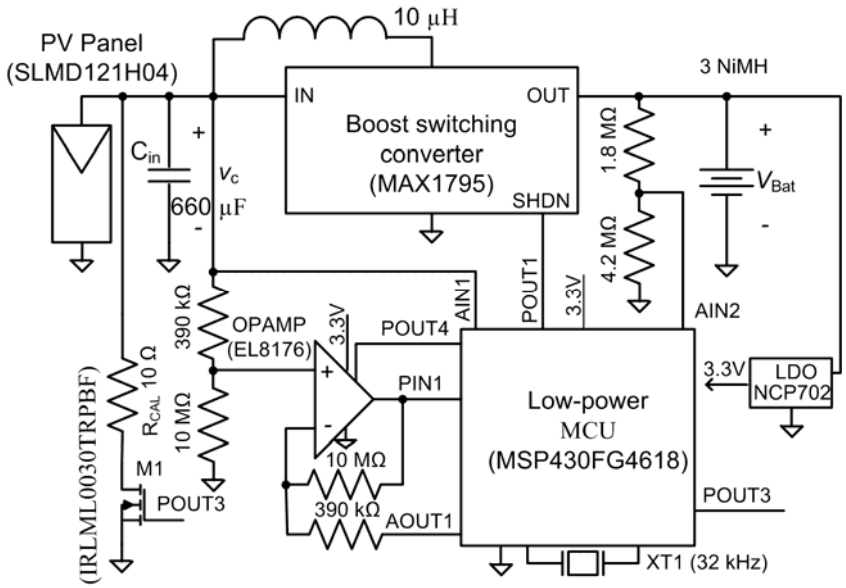

Fig. 8. Circuit diagram of the MPPT system implemented.

Fig. 9 shows the timing diagram of the MPPT circuit. The central processing unit (CPU) of the MCU, the OPAMP and the switching converter are dynamically enabled/disabled through POUT4 and POUT1 to reduce power consumption.

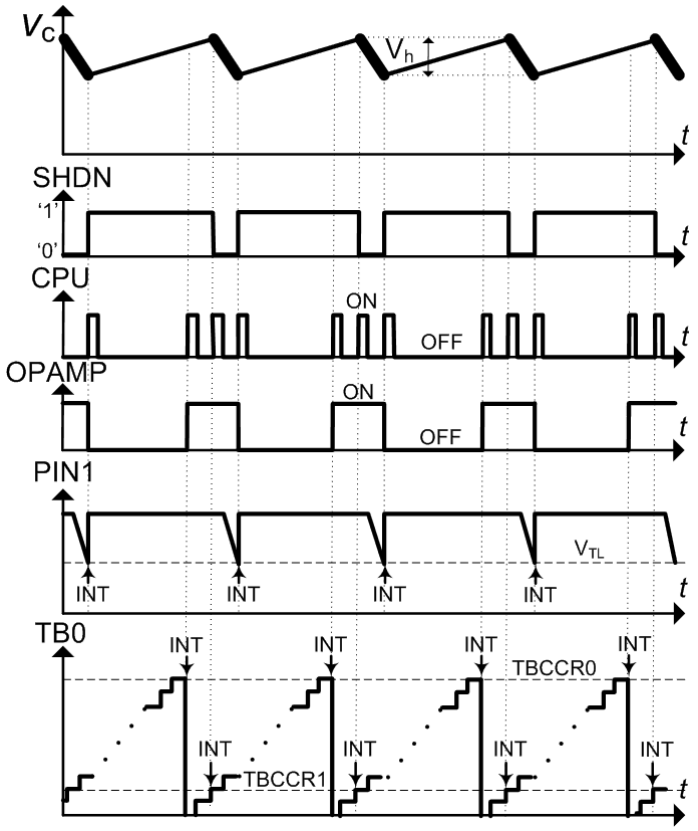

Fig. 9. MPPT timing diagram showing the activity of CPU, timer B0 (TB0), op amp and switching converter.

A timer (TB0) driven by the low-power clock (XT1) issues two interrupt services. The first interrupt, issued when TB0 rolls from TBCCR0 to zero, activates the op amp for a short time before starting each discharge cycle. The second interrupt is issued when TB0 reaches TBCCR1 and starts the discharge cycle. We selected TBCCR1 = 6 to let a wakeup time limit of 183 μs for OPAMP, and to perform the overall calculation to set the next values of TBCCR0. TBCCR0 is periodically updated every 8 charge/discharge cycles to fix the hysteresis window of v_c (V_h) to a desired value (V_{hRef}). If V_h is assumed to be proportional to the duration of the charge states, about TBCCR0 + 1 times the clock period, the following relation can be used,

$$\mathrm{TBCCR0}[n] = (\mathrm{TBCCR0}[n-1]+1)\frac{\mathrm{V_{hRef}}}{\mathrm{V_h[n-1]}} - 1 \tag{3}$$

where n is the current cycle and n - 1 is the previous one.

Another interrupt service disables the switching converter when PIN1 reaches the low threshold of the digital input port at the end of each discharge cycle. PIN1 is the output of the voltage comparator (EL8176 and resistors) and falls down when v_c reaches the low discharge limit.

V_{oc} is sampled after an integer number of charge/discharge cycles equivalent to an elapsed fixed sampling time (T_{oc}) (Fig. 10). During V_{oc} sampling state, the switching converter is disabled for five consecutive interrupt services (TBCCR0) before the new value is measured to calculate V_{MPP} (= KV_{oc}).

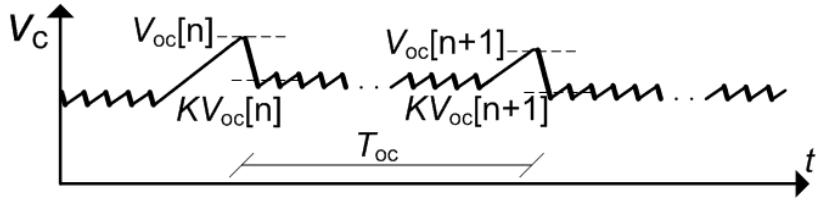

Fig. 10. Timing diagram of V_c showing the periodical update of V_{oc} and the bias voltage of the PV panel (KV_{oc}).

I_{MPP} is estimated from the duration of consecutive charge (t_{CH}) and discharge (t_{DS}) cycles. The measurement is performed during the second charge/discharge cycle immediately after sampling V_{oc}, as shown in Fig. 11. C_{in} is charged by I_{MPP} and afterwards discharged through transistor M1 and reference resistor R_{CAL}. Before starting each charge cycle, C_{in} is briefly discharged to prevent the switching converter from disturbing the measurement. Equating the perturbation of the voltage drop in the input capacitor (V_{hm}) during both cycles yields

$$I_{MPP} = \frac{V_{hm}}{2R_{CAL}}\frac{t_{DS}}{(t_{DS}+t_{CH})} \tag{4}$$

which does not depend on C_{in} hence it is insensitive to its tolerance and temperature and time drifts. V_{hm} is measured by sampling v_c through AIN1 at the beginning (PIN1 INT) and at the end (TB0 INT) of t_{CH}.

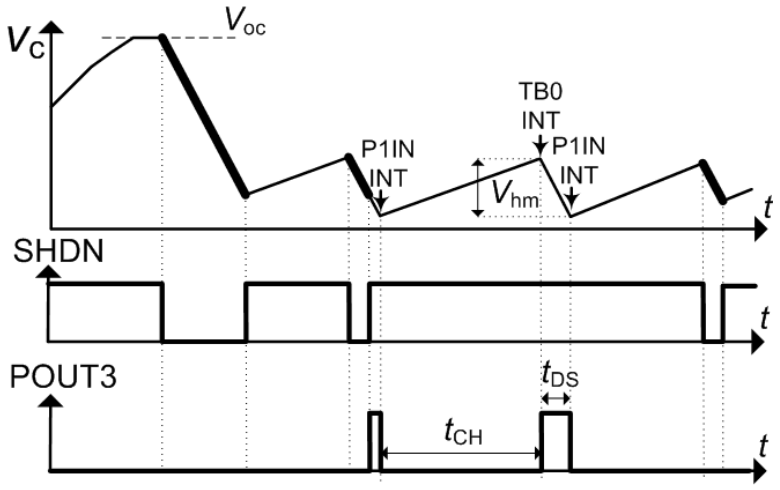

Fig. 11. Timing diagram of the activity to measure I_{MPP} by applying (4).

3. Experimental Results and Discussion

A prototype of the circuit shown in Fig. 8 was implemented in order to assess its performance both as energy harvester and solar irradiance sensor in the laboratory and in the field. MCU and OPAMP were powered by a low-power LDO (NCP702SN33) supplied from NiMH batteries. From the experimental *P*/*V* curve, we determined that the best constant (*K*) to achieve maximum energy was 0.81.

In order to achieve reproducible laboratory measurements, the PV panel (SLMD121H04) was first illuminated by a high power LED (BXRA-C1202), the batteries were replaced by a voltage power supply and the average power consumption of the overall system was measured as a function of the incoming power on the PV panel (Fig. 12). This power does not account for power losses in the switching converter and was estimated by multiplying the input current of the LDO and the battery voltage (4 V). As the activity of the switching converter, MCU and OPAMP increases for higher PV power, power consumption increases for increasing power. Notice that the resulting power is always lower than the sum of the power consumption of each component of the circuit when they are continuously active (∼17 mW). Dynamic reconfiguration algorithms that deactivate each unused component, prevents reaching this power threshold.

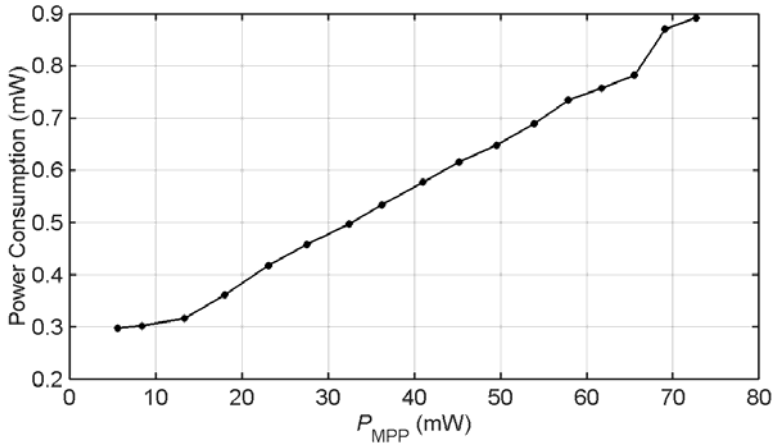

Fig. 12. Power consumption versus incoming power of the PV panel.

The efficiency of MPPT (η), defined as the ratio between the power delivered to the batteries and P_{MPP}, was also measured in the laboratory (Fig. 13). η is limited by several factors: power consumption (Fig. 12), switching converter efficiency, power lost during the sampling period of V_{oc}, t_{CH} and t_{DS}, deviation between the actual V_{MPP} and that calculated from the empirical relation $V_{MPP} = KV_{oc}$, and the deviation of PV panel bias voltage from V_{MPP} caused by the hysteresis window ($V_{h)}$. All these factors become more relevant for smaller P_{MPP} and as a result η is only 78.4% at P_{MPP} = 5.4 mW and increases up to 87% at P_{MPP} = 61.7 mW.

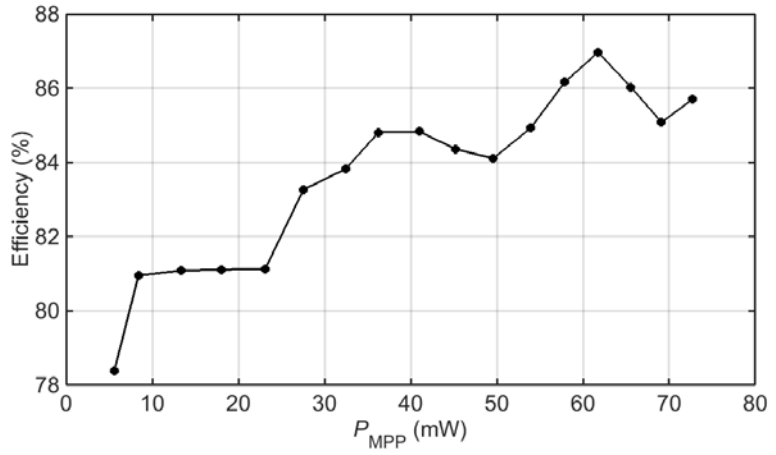

Fig. 13. Efficiency (η) of the energy harvester versus the incoming power of the PV panel.

Field measurements were performed in November and December 2017 at our university campus (41˚16'N, 1˚59'E) to observe the measurement accuracy of the solar irradiance sensor. The PV panel was

placed on a horizontal plane and a nearby second class thermopile pyranometer, (HD52.3DP147, Delta Ohm) was used as a reference. Data was recorded under several meteorological conditions wherein both sensors received direct and indirect light because of environmental shadows projected onto the sensors.

Fig. 14 shows the irradiance measured by the reference pyranometer (G_{ref}) during two days that correspond to extreme situations. At sunrise (8:00 am) a nearby building projected a shadow until 11:45 am so that the measured irradiance was low. Afterwards, irradiance rose up in the sunny day and followed the cosine function of sun's zenith angle. Lower irradiances were measured during a cloudy day and followed a random function that corresponds to light attenuation due to clouds.

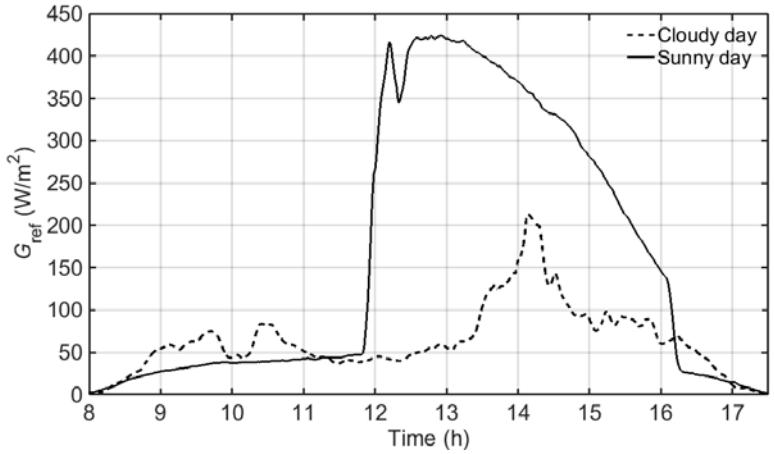

Fig. 14. Irradiance measured by a HD52.3DP147 pyranomenter during a sunny and a cloudy day.

Fig. 15 shows I_{MPP}(25 ºC) measured by the system using relations (2) and (4) during the two same days. Time evolutions of I_{MPP}(25 ºC) and G_{ref} were quite similar.

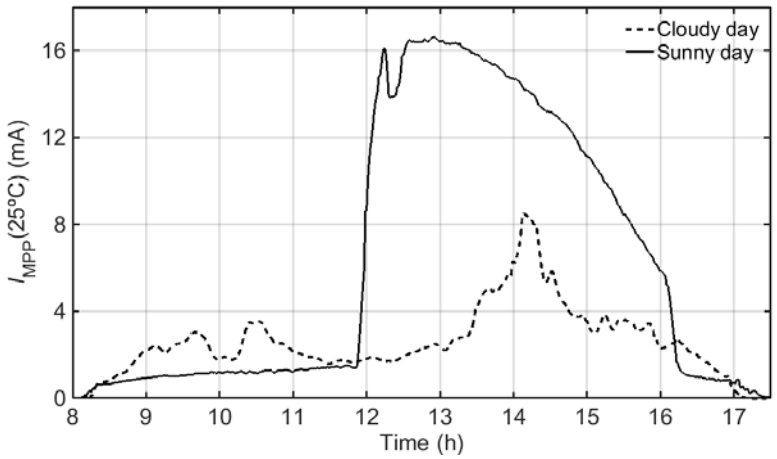

Fig. 15. I_{MPP}(25 ºC) measured during a sunny and a cloudy day.

The relation between G_{ref} and I_{MPP}(25 ºC) for several days is shown in Fig. 16. Data points obtained around 11:45 am were removed because a brief delay in the shadow projected on both sensors yields a significant difference in the respective incident irradiances that cause false estimation errors. For the other data points, an almost linear relation is obtained whose slope deviates up to ±2.4 % depending on light spectra. A nonlinear behavior can also be observed at irradiances below 50 W/m^2 that can be attributed to the nonlinear relation already observed in Fig. 4, light reflection and absorption on PV panel's surface at sunrise and sunset (cosine error).

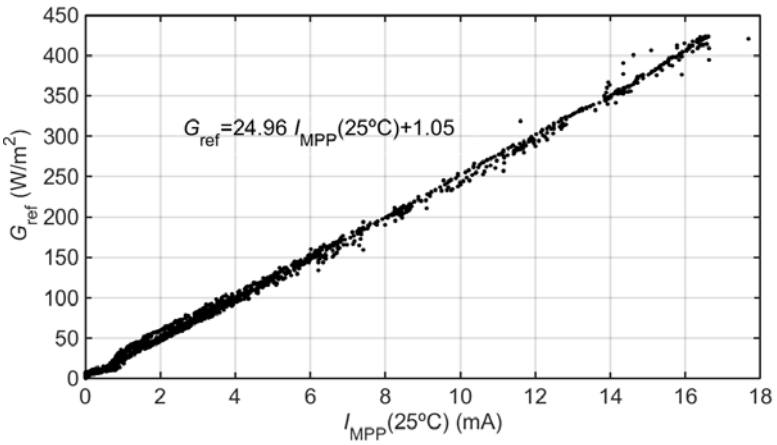

Fig. 16. G_{ref} versus I_{MPP}(25 ºC) obtained during several days and the resulting linear regression.

The coefficients of a linear calibration curve were obtained by linear regression (Fig. 16). The resulting root mean square deviation from the straight line is 4.85 W/m^2. Fig. 17 and Fig. 18 compare G_{ref} to the irradiance estimated from I_{MPP}(25 ºC) using that calibration curve. Note that measurement deviation increases up around 11:45 am in a sunny day when shadow is projected on the PV panels and the reference pyranometer. Outside this time interval, the deviation is below 15 W/m^2.

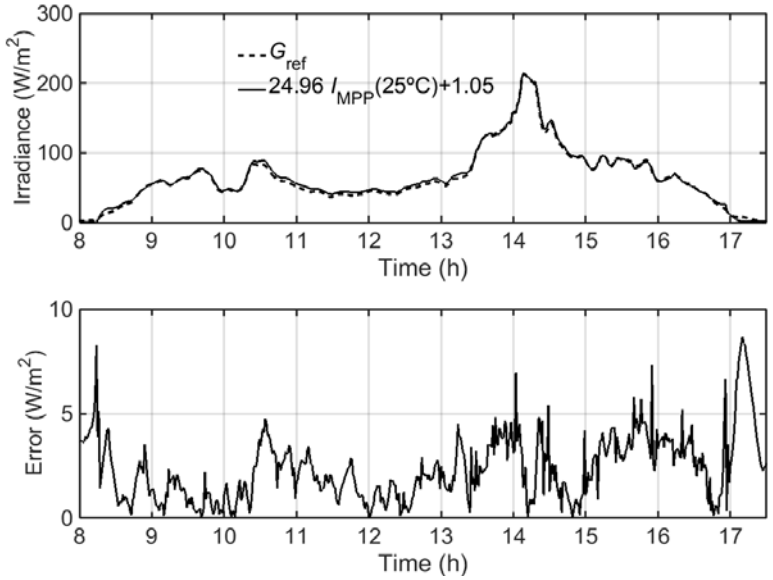

Fig. 17. Comparison between measured and reference irradiance during a cloudy day.

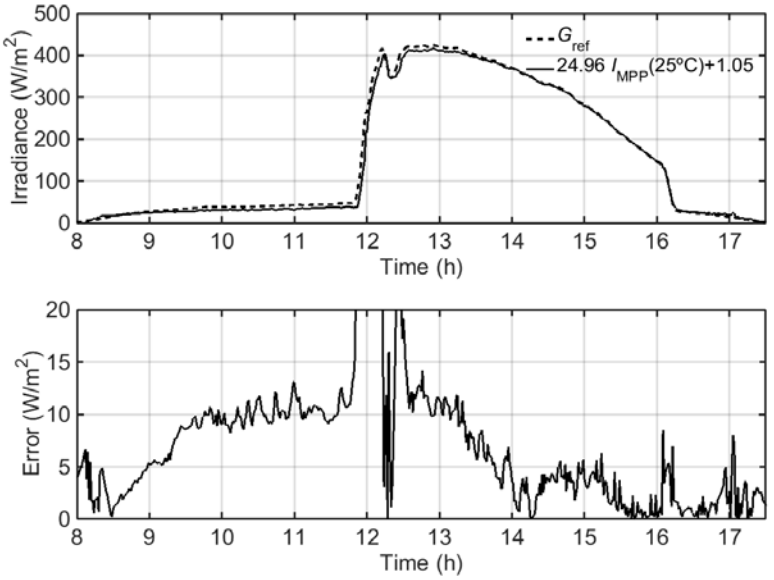

Fig. 18. Comparison between the measured and the reference irradiance during a sunny day.

Daily solar insolation was calculated from the data obtained from the reference pyranometer and the irradiance sensor designed. The maximum relative deviation of daily solar insolation was obtained in a cloudy day and was below ±3.6 %. This causes relatively small changes in infection risk of fungus diseases assessment and to estimate evapotranspiration. (Llasat and Snyder, 1998) reported that daily insolation overestimation by 4 % causes an error in the potential evapotranspiration of between 1.6 % and 3.6 %.

Several silicon low-cost pyranometers are available in the market that suit these applications and can be

compared with the proposed design. Some examples are S-LIB-M003 (Inset Hobo), SP-100-SS (Apogee), SP-Lite 2 (Kipp&Zone) and LP Silicon PYRA 04 (Delta Ohm). Their spectral sensitivity is similar to the proposed sensor in the range from 300 nm to 1100 nm and compensate for temperature drift. However, they provide Teflon diffusers to achieve cosine error bellow ±5% for incident angles between 0º and 75º. Obviously this improves measurement accuracy for high incident angles (during sunrise and sunset) but daily solar irradiation measurement does not improve significantly. Moreover, attaching a Teflon diffuser to the PV panel attenuates the incident irradiance and hence the energy harvested. On the other hand, the proposed design adds about 0.5 € extra cost to the hardware of the sensor node, well below the cost of commercial silicon pyranometers (above 200 €).

4. Conclusions

Solar radiation energy in low-cost and low-power autonomous sensor nodes can be estimated from the PV solar energy harvester in the node. Since parts of the solar energy harvester and the MCU of the sensor node are also used to implement the sensor, only an extra-low-power MOSFET and a resistor are needed. By taking advantage of the inherent operation of FOCV PFM MPPT, V_{oc} sampling and the duration of the charge and discharge states are used to estimate solar irradiance with temperature drift compensation. A prototype, implemented to assess its performance both as energy harvester and solar radiation sensor, has achieved a power efficiency comparable to commercial low-power solar energy harvesters IC, such as BQ25504 and ADP5090, and daily solar insolation deviation is below ±3.6%. This error is similar to that of commercial photodiode-based pyranometers which exhibit similar spectral response uncertainty but, in contrast to the proposed sensor, include optical diffusers to avoid light reflection and absorption. This error, however, has limited effect on the assessment of infection risk of fungus diseases and to estimate evapotranspiration estimation.

References

Carrasco, M., Mancilla-David, F., Ortega, R., 2014. An estimator of solar irradiance in photovoltaic arrays with guaranteed stability properties. IEEE Trans. Ind. Electron. 61, 3359–3366. https://doi.org/10.1109/TIE.2013.2281154

da Costa, W.T., Fardin, J.F., Machado Neto, L. de V.B., Simonetti, D.S.L., 2014. Estimation of irradiance and temperature using photovoltaic modules. Sol. Energy 110, 132–138. https://doi.org/10.1016/j.solener.2014.08.040

Dalla Marta, A., Di Stefano, V., Cerovic, Z.G., Agati, G., Orlandini, S., 2008. Solar radiation affects grapevine susceptibility to Plasmopara Viticola. Sci. Agric. 65, 65–70. https://doi.org/10.1590/S0103-90162008000700011

Gocić, M., Motamedi, S., Shamshirband, S., Petković, D., Ch, S., Hashim, R., Arif, M., 2015. Soft computing approaches for forecasting reference evapotranspiration. Comput. Electron. Agric. 113, 164–173. https://doi.org/10.1016/j.compag.2015.02.010

Husain, N.S., Zainal, N.A., Mahinder Singh, B.S., Mohamed, N.M., Mohd Nor, N., 2011. Integrated PV based solar insolation measurement and performance monitoring system, in: 2011 IEEE Colloquium on Humanities, Science and Engineering, CHUSER 2011. pp. 710–715. https://doi.org/10.1109/CHUSER.2011.6163827

Katsantonis, D., Kadoglidou, K., Dramalis, C., Puigdollers, P., 2017. Rice blast forecasting models and their practical value: A review. Phytopathol. Mediterr. 56. https://doi.org/10.14601/Phytopathol_Mediterr-18706

Kipp&Zonen, 2018. Products: Pyranometers [WWW Document]. URL http://www.kippzonen.com/ProductGroup/3/Pyranometers (accessed 8.20.01).

Llasat, M.C., Snyder, R.L., 1998. Data error effects on net radiation and evapotranspiration estimation. Agric. For. Meteorol. 91, 209–221. https://doi.org/10.1016/S0168-1923(98)00070-7

Ma, J., Bi, Z., Shi, Y., Man, K.L., Pan, X., Wang, J., 2017. OL-SVR based soft-sensor for real-time

estimation of solar irradiance, in: 2016 IEEE Asia Pacific Conference on Circuits and Systems, APCCAS 2016. pp. 448–451. https://doi.org/10.1109/APCCAS.2016.7803999

Mancilla-David, F., Riganti-Fulginei, F., Laudani, A., Salvini, A., 2014. A neural network-based low-cost solar irradiance sensor. IEEE Trans. Instrum. Meas. 63, 583–591. https://doi.org/10.1109/TIM.2013.2282005

Ortiz Rivera, E.I., Peng, F.Z., 2006. Algorithms to estimate the temperature and effective irradiance level over a photovoltaic module using the fixed point theorem, in: PESC Record - IEEE Annual Power Electronics Specialists Conference. https://doi.org/10.1109/PESC.2006.1711792

Petković, D., Gocic, M., Trajkovic, S., Shamshirband, S., Motamedi, S., Hashim, R., Bonakdari, H., 2015. Determination of the most influential weather parameters on reference evapotranspiration by adaptive neuro-fuzzy methodology. Comput. Electron. Agric. 114, 277–284. https://doi.org/10.1016/j.compag.2015.04.012

Reuter, H.I., Kersebaum, K.C., Wendroth, O., 2005. Modelling of solar radiation influenced by topographic shading - Evaluation and application for precision farming. Phys. Chem. Earth 30, 143–149. https://doi.org/10.1016/j.pce.2004.08.027

Wang, N., Zhang, N., Wang, M., 2006. Wireless sensors in agriculture and food industry - Recent development and future perspective. Comput. Electron. Agric. https://doi.org/10.1016/j.compag.2005.09.003